Unraveling the origins of ferroelectricity in doped hafnia through carrier-mediated phase transitions

Check for updates

Gang Li[1,2,8], Shaoan Yan[2,8], Yulin Liu[3], Wanli Zhang[4], Yongguang Xiao[3], Qiong Yang [3], Minghua Tang [3,5] ✉, Jiangyu Li[6,7] ✉ & Zhilin Long[1] ✉

Doping is critical for inducing ferroelectricity in hafnia films, yet the underlying mechanisms remain debated. Here, through first-principles studies, we elucidate the pivotal role played by the complex phase transition mechanisms under carrier doping in understanding the origin of hafnia ferroelectricity. Specifically, electron doping orchestrates a metastable polar phase to stable antipolar phase transformation, driven by strong screening effects and weakened nonpolar covalent bonds, making n-type dopants rare. Conversely, weak screening effect and enhanced polar covalent bonding strengthen robust ferroelectricity, enabling significant ground-state phase transitions from the monoclinic to the polar orthorhombic phase and finally to the cubic phase under hole doping, a phenomenon prevalent in hafnia-based films doped with p-type dopants. Furthermore, this hole-enhanced polar distortion also results in an inverse size effect in hafnia ferroelectric films, unlike perovskite ferroelectrics. Our findings offer new insights into the preparation of robust hafnia-based ferroelectric films through doping or interface engineering.

After the discovery of ferroelectricity in doped HfO_2 and $(Hf,Zr)O_2$ (HZO) thin films[1,2], they have drawn widespread attention for the next-generation nanoscale devices. This interest arises from their full compatibility with the complementary metal-oxide-semiconductor (CMOS) process, coupled with their excellent retention and scalability[3–5]. Unfortunately, the stable phase of bulk HfO_2 and ZrO_2 at room temperature and ambient pressure is monoclinic phase (m, $P2_1/c$)[6,7]. At high-temperature, the stable phase transforms into the tetragonal (t, $P4_2/nmc$) phase and cubic phase (c, $Fm\bar{3}m$), while at high pressure, it changes into the antipolar orthorhombic phase (o, Pbca)[6]. Since the orthorhombic ferroelectric phase (f, $Pca2_1$) is absent in phase diagrams, it is crucial to determine the possible thermodynamic and kinetic driving factors behind the formation of this unexpected ferroelectric f-phase.

Doping with various cations or nitrogen is recognized as a pivotal method for inducing and controlling ferroelectricity in HfO_2 and HZO thin films[8–13], encompassing synergistic interplay among factors such as oxygen vacancies[14–16], surface energy[17,18], and stress and strain[19,20]. Theoretical predictions[21,22] and experiments[11,23,24] have verified that dopants with larger ionic radius and lower electronegativity are more effective in stabilizing ferroelectric f-phase at appropriate concentrations. Excessive doping reduces the f-phase fraction by weakening the transition from the t-phase during rapid thermal annealing, favoring the dominance of the t-phase[25,26]. Notably, a closer examination of the dopants that stabilize the f-phase of hafnia reveals a common characteristic: they are typically p-type dopants (Ca, Sr, Al, Y, La, Gd, etc), which inevitably introduce holes into the crystal. Interestingly, experiments unexpectedly found that ferroelectricity in n-type Ta-doped HfO_2 films[27] occurs only at high concentrations, with no current explanation for this observation. Unfortunately, the roles played by the carriers introduced by these dopants are often overlooked.

Ferroelectric (polar) metals have recently become a research hotspot due to their potential to elucidate the mechanism underlying the coexistence of two seemingly incompatible properties: ferroelectricity (polarity) and metallicity[28–31]. Experimental findings have identified a critical electron concentration in n-type $BaTiO_3$-based ferroelectric-like metals[32]. Theoretical insights suggest that the persistence of polar distortion is linked to the incomplete screening of Coulomb forces within this concentration range[33].

[1]College of Civil Engineering, Xiangtan University, Xiangtan, China. [2]School of Mechanical Engineering and Mechanics, Xiangtan University, Xiangtan, China. [3]School of Materials Science and Engineering, Xiangtan University, Xiangtan, China. [4]Key Laboratory of Micro Nano Optoelectronic Devices and Intelligent Perception Systems, Yangtze Normal University, Chongqing, China. [5]The National Center for Applied Mathematics in Hunan, Xiangtan University, Xiangtan, China. [6]Department of Materials Science and Engineering, Southern University of Science and Technology, Shenzhen, China. [7]Guangdong Provincial Key Laboratory of Functional Oxide Materials and Devices, Southern University of Science and Technology, Shenzhen, China. [8]These authors contributed equally: Gang Li, Shaoan Yan. ✉e-mail: tangminghua@xtu.edu.cn; lijy@sustech.edu.cn; longzl@xtu.edu.cn

Other interaction mechanisms also include the meta-screening effect and chemical bonding, which anomalously enhance the ferroelectricity of perovskites with carrier doping[34–36]. Recent studies have realized the crucial role played by holes introduced by dopants[37] or interface engineering[38] in stabilizing f-phase HfO$_2$. Nevertheless, the true microscopic mechanisms through which carriers introduced by dopants stabilize the metastable f-phase remain elusive.

In this letter, we perform a first-principles analysis of the evolution of crystal structure, electronic structure, and chemical bonds in the various phases of hafnia under carrier electrostatic doping. Notably, our analysis intentionally disregards interference from intrinsic properties of the dopant, such as ionic radius and electronegativity. Our findings reveal that carrier-doped hafnia undergoes intricate phase transitions, posing challenges in unequivocally identifying the ferroelectric nature of the material. The presence of multiple coexisting phases, driven by small energy differences, further complicates this identification. Remarkably, the phase transitions contribute to the enhancement of f-phase stability at a specific concentration in the case of p-type doping, while n-type doping proves to be more challenging. To elucidate this phenomenon, we examine the interplay between carriers and ferroelectricity in terms of both screening effects and chemical bonds.

For p-type doping, polar triply coordinated oxygen (O^{III}) and nonpolar quadruply coordinated oxygen (O^{IV}) assume distinctive roles, where the presence of a hole on the O^{IV} atom significantly impacts the total energy of each phase, whereas a hole on O^{III} atoms stabilizes the polar distortion by reinforcing the Hf-O^{III} covalent bond. Consequently, hafnia undergoes a sequence of ground-state phase transitions (m → f → c) with an increasing hole concentration. This evolving pattern of phase transition closely parallels observations in La-doped and Y-doped HfO$_2$ thin films[12,23]. Conversely, n-type doping follows an opposite mechanism due to the strong screening effect and the instability of the Hf-O^{IV} covalent bond. This drives the metastable f-phase towards destabilization and ultimately leads to phase transitions to the stable antipolar Pbcn phase with increasing electron concentration. This mechanism can be indirectly confirmed by Ta-doped HfO$_2$ films[27], since the remanent polarization P_r is almost identical to theoretical predictions.

These unconventional concepts might appear perplexing at first, particularly considering the inherent challenge of measuring ferroelectric properties in metals. To address this, we draw comparisons between the electronic characteristics of SiO$_2$/HfO$_2$-based heterostructures with and without TiN electrodes. Our speculation is grounded in the idea that carriers play a preferential role in fostering the formation of the f-phase. The rationale behind this lies in the fact that, when capped with electrodes, carriers are directed toward the electrode material, ensuring ferroelectric insulation. This rationale sheds light on why a 1 nm ultrathin HZO layer without a metal capping layer does not exhibit ferroelectric signatures, but displays such signatures when paired with a metal capping layer[39]. Our results are consistent well with the existing experimental results, demonstrating that our work resolves the mystery of the origin of ferroelectricity in doped hafnia and suggests manipulating carriers as a universal strategy to tune ferroelectricity in hafnia.

Results and discussions
Rich phase transition under carrier conditions
In Fig. 1a, all O^{IV} atoms in the high-symmetry c-phase and t-phase are equivalent, exhibiting a nonpolar nature. The O^{IV} atoms in the non-centrosymmetric f-phase are equivalent, and polarization in the f-phase originates from the motion of O^{III} atoms upon polarization switching along the c-direction. The antipolar o-phase can be conceptualized as the O^{III} polarization reversal of neighboring unit cells in the f-phase. Consequently, the energy difference between the two phases is minimized, allowing for a facile transformation from the o-phase to the f-phase under the influence of an external electric field[40]. Due to this characteristic, the o-phase is often overlooked in theoretical calculations. Interestingly, although the lower symmetry m-phase features polar O^{III} atoms and boasts the lowest energy,

its overall behavior remains nonpolar. This nonpolar nature is attributed to its inability to form a long-range polar order arrangement.

In Fig. 1b, c, carriers profoundly influence the total energy of the various phases of hafnia. Observing the abrupt changes in the total energy of certain phases with increasing carrier concentration is more intuitively reflected in the sudden alterations of phase lattice parameters. These changes imply the occurrence of structural phase transitions. The multitude of phase transitions, coupled with the inherent complexity of the original multiple-phase structures, adds intricacy to the analysis of doped hafnia. In general, hole doping and electron doping contribute to increased stability and instability of the phase structure, respectively.

In Fig. 1b, it is evident that phases with higher symmetry exhibit initially steeper slopes in the decrease of total energy. Consequently, the c-phase, characterized by the highest symmetry, demonstrates the most pronounced decrease slope (Supplementary Fig. 1a). Throughout this progression, the t-phase gradually undergoes transformation into the c-phase. This transformation is visually apparent in Fig. 1d, where the lattice constant of the t-phase gradually diminishes until it aligns with that of the c-phase, occurring at a critical concentration ($p = 0.16\ h^+$/f.u.). Surprisingly, the m-phase undergoes a structural phase transition to the new high-symmetry phase (m′, space group: Pbcm) at $p = 0.37\ h^+$/f.u., reverting to the ground state with a steeper slope than the c-phase (Supplementary Fig. 1a). This transition is marked by a significant change in the lattice parameter lattice parameter β, shifting abruptly from a non-right angle to a right angle (Fig. 1g). The m′-phase is recognized as an intermediate transition structure in the polarization switching process in many theoretical calculations[40,41]. In addition, the low-symmetry f-phase and o-phase undergo a structural phase transition to high-symmetry c-phase (Fig. 1e) and m′-phase (Supplementary Fig. 2d) at higher hole concentrations. Upon comparing the total energy descending slopes of the c-phase and m'-phase, it becomes apparent that symmetry under hole doping may not be the primary determinant of the total energy change in each phase.

Comparing the total energies of these doped phase structures, HfO$_2$ undergoes ground-state phase transitions of m → f (o) → c (t) → m′, respectively. This sequence of phase transitions aligns with observations in La-doped HfO$_2$ thin films[23]. In experiments with increasing La doping concentration, the highest phase fractions in the GIXRD patterns exhibit m → f → c phase structures. The unexpected emergence of the m′-phase following the c-phase at high concentrations naturally would not receive much attention in experiments. Additionally, since our doping approach ignores the physical properties of the dopant atoms, experiments have demonstrated that smaller and larger dopants generally induce the t-phase and c-phase in HfO$_2$, respectively[42], so that the t-phase dominates at high Al doping concentrations.

Turning attention to ferroelectric f-phase, the energy difference between the f-phase and m-phase gradually decreases with the increase of hole concentration (Supplementary Fig. 3a). Notably, when the hole concentration reaches 0.16–0.26 h^+/f.u. (the inset of Fig. 1b), the total energy of the f-phase becomes the lowest, signifying that suitable hole concentration can indeed stabilize the f-phase. These findings are consistent with theoretical predictions suggesting that p-type elements are the most suitable dopants for promoting ferroelectricity in hafnia, corroborated by the large remanent polarization measured in hafnia films doped with these elements[21]. It's worth noting that the actual dopant may have varying effects on the crystal structure of each phase. Theoretical calculations have not identified a scenario where the dopant alone can stabilize the f-phase as the ground state[21].

The reduction in lattice constants b and c is not significant in Fig. 1e. However, due to the rapid decrease in lattice constant a, thereby reducing the volume with increasing hole concentration[23]. These changes in the longest lattice constants are much stronger than that of the two shorter axes lattice constants, which can be found in Al- and Gd-doped HfO$_2$ thin films[11]. Another crystallographic signature worth noting is the aspect ratio $2a/(b + c)$, akin to perovskite tetragonality (c/a)[43]. The aspect ratio exhibits a decreasing trend from 1.04 to 0.95 with increasing hole concentration
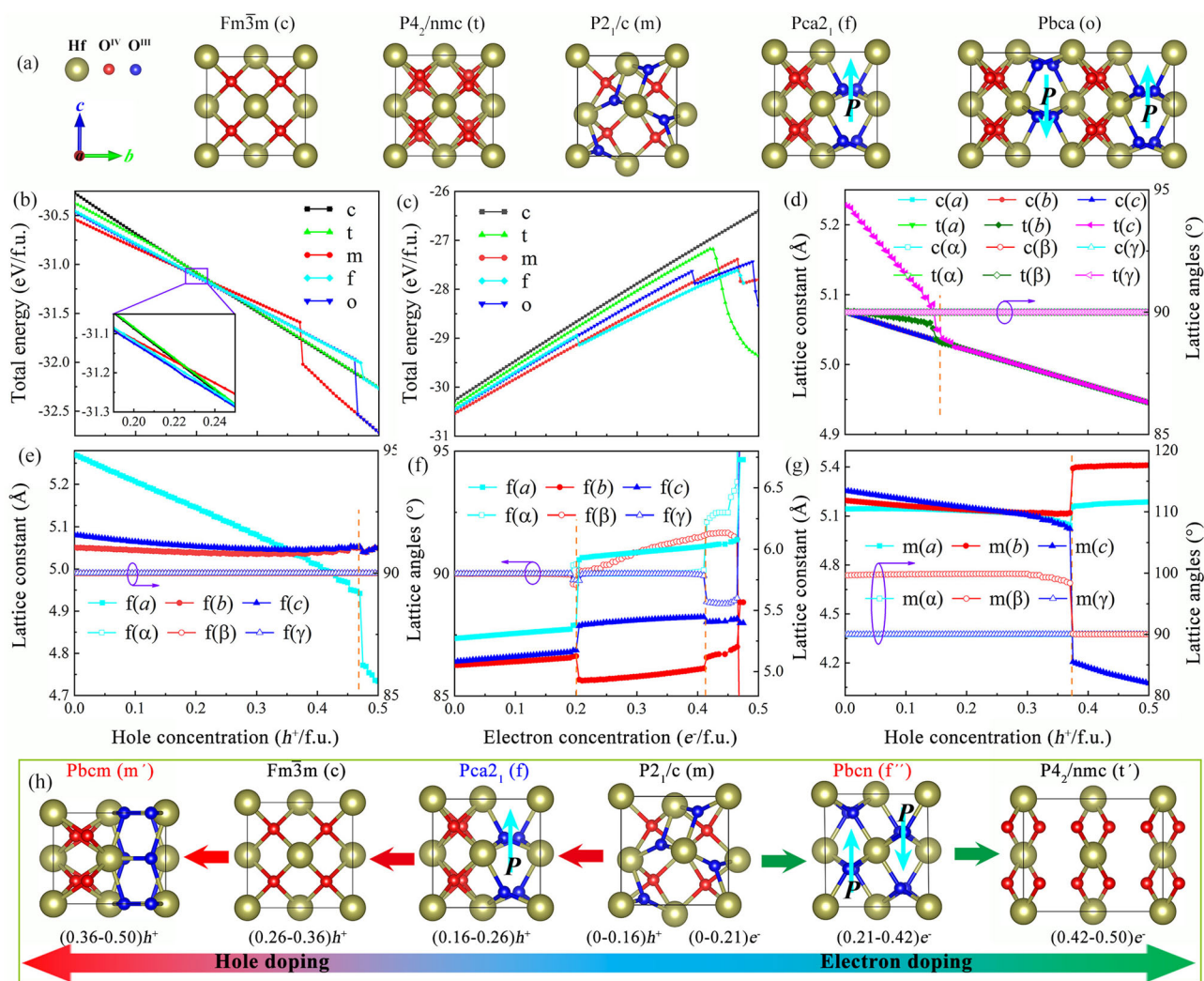
Fig. 1 | Phase structure evolution with carrier doping. a Crystal structures of the bulk HfO_2 with different phases, red and blue balls indicate quadruply coordinated (O^{IV}) and triply coordinated (O^{III}) oxygen, the cyan arrow is the direction of polarization. The total energy with different phases as a function of (**b**) hole and (**c**) electron concentration, the inset in (**b**) shows that the f-phase with the lowest total energy. The lattice parameters (a, b, c, α, β, γ) of the bulk HfO_2 as a function of the carrier concentration, (**d**) hole-doped c (t)-phase, (**e**) hole-doped f-phase, (**f**) electron-doped f-phase, (**g**) hole-doped m-phase. The vertical orange-yellow dashed line indicates that the structural phase transition occurs here. **h** A conceptual phase diagram of carriers doped of bulk HfO_2, the stable crystal structure corresponding to different carrier concentrations is determined based on total energy and lattice parameters, the new Pbcm and Pbcn space groups originate from structural phase transitions of m- and f-phase, respectively.

(Supplementary Fig. 4), mirroring observations observed in La-doped HfO_2 thin films, where the aspect ratio decreases from 1.03 to 0.98 with increasing La content[23]. The aspect ratio is smaller than the ideal value 1, a phenomenon previously attributed to the larger biaxial in-plane tensile stress[23,44,45]. However, our prediction attributes the change in aspect ratio to the evolution of lattice constants resulting from hole doping. At high hole concentrations, the lattice constants $b = c \neq a$ (Fig. 1e), indicating that the f-phase eventually transforms into a pseudo-cubic phase (Supplementary Fig. 4).

In contrast to hole doping, the energy difference between the phases with higher symmetry and the m-phase increases with growing electron doping concentration (Supplementary Fig. 3b). Judging from the increase of lattice constants under electron doping (Fig. 1f and Supplementary Fig. 2), the structures of HfO_2 become progressively unstable. Particularly noteworthy is the behavior of the t-phase under high electron doping, the long Hf-O^{IV} bonds break, causing a rapid increase in the lattice constant c ($c > 10$ Å), ultimately resulting in the formation of a ground-state 2D structure (Supplementary Fig. 2a). To distinguish it from the original t-phase, it is named t'-phase (Fig. 1h).

Luo et al.[27] discovered n-type Ta-doped HfO_2 films exhibited only the presence of the m-phase at low Ta concentrations (<11%, much larger than p-type dopants), without evidence of f-phase/t-phase coexistence. This observation will not appear in p-type doped HfO_2 films, however, it supports our prediction that the energy difference between the f-phase/t-phase and the m-phase increases at low electron concentration (Supplementary Fig. 3b), reducing the likelihood of f-phase/t-phase formation. As another empirical demonstration, Xu et al.[46] experimentally showed that pentavalent Nb doping (<3%) stabilizes the m-phase of HfO_2 thin films more than dopants like N, Zr, Sc, and Y, increasing the m-phase fraction to 100%. At a high Ta doping concentration (16%), the m-phase is suppressed, and the f-phase eventually becomes dominant in the XRD patterns. At this point, the remanent polarization P_r can reach up to 53 $\mu C/cm^2$ is nearly equal to our predicted 58 $\mu C/cm^2$. This is also in line with our predictions, that is, the f-phase unexpectedly undergoes a structural phase transition, giving rise to a new ground-state phase with space group Pbcn (f″).

The f″-phase of HfO_2 primarily emerges under large tensile strain ($\varepsilon > 3\%$)[47], aligning with the observed large lattice constant at high electron concentrations (Fig. 1f). Examining its crystal structure as shown in Fig. 1h,
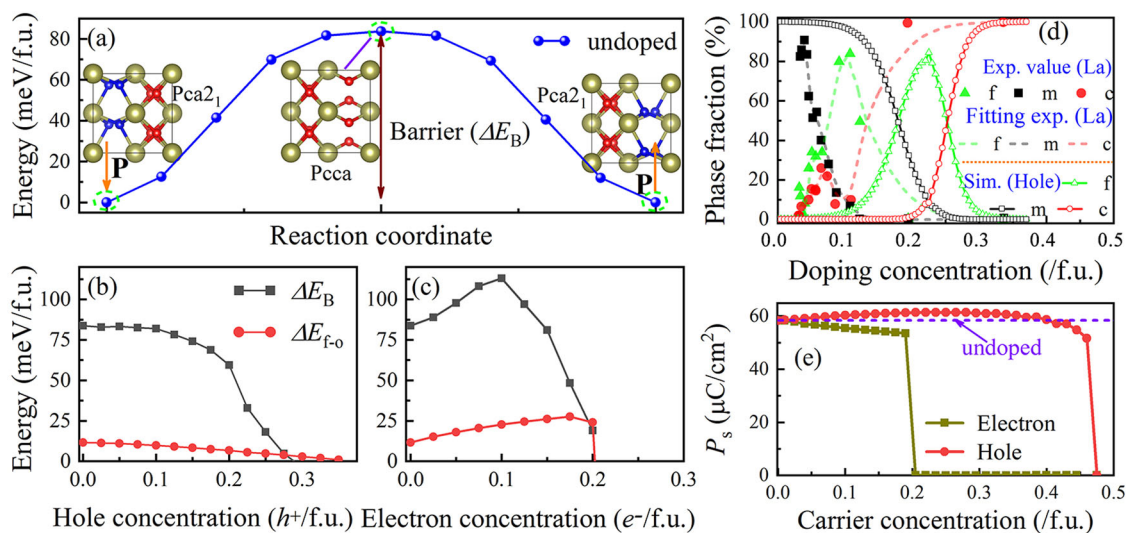
Fig. 2 | Effects of carriers on ferroelectricity. a Energy landscape in the process of structure transition from polarization-down to polarization-up of the undoped f-phase HfO$_2$. Points marked with green dashed circles indicate the energies of the initial, transition, and final states, and purple arrows indicate the polarization switching barrier (ΔE_B), the intermediate transition phase adopts the Pcca phase. Barrier (ΔE_B) and energy difference ($\Delta E_{f-o} = E_f - E_o$) between the f-phase and o-phase as a function of (**b**) hole and (**c**) electron concentration. **d** Relative f-, m-, and c-phases fraction as a function of doping concentration, the La-doped HfO$_2$ thin films as a reference [ref. 23]. **e** The spontaneous polarization magnitude of the f-phase HfO$_2$ as a function of the carrier concentration.

nonpolar O^{IV} atoms become polar O^{III} atoms, but the polar direction is diametrically opposite to the original O^{III}, resulting in an antipolar configuration. Theoretical calculations by Zhou et al.[48] reveal that polar-antipolar coupling is the origin of ferroelectricity in HfO$_2$ with large tensile strain. Moreover, Choe et al.[49] found that compared with the t-phase, the f″-phase acts as an intermediate transition phase for polarization switching, with an ultralow energy barrier for the domain wall switching.

The t-phase is widely considered a precursor phase for crystalline annealing of HfO$_2$ ferroelectric films, which induces a kinetically driven t-phase to f-phase transition during the annealing and cooling process. Through climbing image nudged elastic band (NEB) calculations[50,51], we found that the energy barrier to be overcome for the transition of the f″-phase to the f-phase is comparable to that for the transition of the t-phase to the f-phase (Supplementary Fig. 5), and significantly lower than that for the transition of the f″-phase to the other (c, t, m) phases. This suggests that the antipolar f″-phase can also transform into the f-phase through thermal annealing. High-temperature annealing under ambient conditions can stabilize the f-phase beyond the critical dopant concentration, as shown by Luo et al.[27] Considering the significant challenges with n-type doping, further experimental validation of the polar-antipolar phase transition is undoubtedly necessary.

Carrier regulates ferroelectric properties

In Fig. 2a, we utilized a NEB to calculate the polarization switching barrier (ΔE_B). A larger ΔE_B indicates more challenging switching polarization, requiring a higher coercive field (E_c)[52,53]. Figure 2b illustrates that ΔE_B first decreases slowly and then decreases rapidly with the increase of hole concentration, indicating that the polarization switching becomes easier, and E_c decreases accordingly. For instance, the E_c drops from 1.35 MV/cm at 5 cat% La to below 1.2 MV/cm at 13 cat% La in the La-doped HfO$_2$ thin films[23]. Additionally, the E_c = 1.2 MV/cm of the HZO film without La doping decreases to E_c = 0.8 MV/cm of the HZO film with La doping[24]. In Fig. 2c, ΔE_B shows an increasing trend followed by a decreasing trend, indicating that polarization switching becomes increasingly difficult at low electron concentrations, but because O^{IV} tends to be unstable under high electron concentrations, the ΔE_B decreases rapidly. Therefore, the coercive field of the 16% Ta-doped HfO$_2$ thin film is relatively small, that is, E_c = 0.8 MV/cm[27]. Recently, Wang et al.[54] discovered rhombohedral ferroelectric Hf(Zr)$_{1+x}$O$_2$ materials with the ultralow coercive field of

E_c = 0.65 MV/cm. which aligns with our prediction our prediction because excess Hf(Zr) atom introduces more electrons than Ta atom. In addition, the energy difference between the f-phase and o-phase (ΔE_{f-o}) decreases with an increasing hole concentration, indicating that the transition from the o-phase to the f-phase becomes easier. This is confirmed by XRD, which shows a phase transition from o-phase to f-phase with increasing Y doping concentration from 8% to 12% in bulk HfO$_2$:Y single-crystalline[12].

The small energy differences between phases commonly result in multiphase coexistence in doped HfO$_2$ thin films[11,23]. In Fig. 2d, the three (m, f, c) phase fractions under the hole concentration were calculated using the Boltzmann distribution, compared with La-doped HfO$_2$ thin film[23]. The f-phase fraction showed first increasing from zero to maximum and then decreasing to zero, which is highly consistent with the experimental results. In addition, the calculated dielectric constant k of multiphase HfO$_2$ the well agrees with the films (Supplementary Fig. 6a). In the case of idealized structures, the suitable concentration range tends to extend beyond what is observed in experimental conditions.

In Fig. 2e, the estimated spontaneous polarization P_s slightly increases (decreases) with the growth of hole (electron) concentration before reaching the critical concentration. Although quantifying the polarization value in metallic materials is uncertain[55,56], the positive correlation between the remanent polarization P_r and the f-phase fraction[23] suggests that P_s persists more or less unaffected by the carrier concentration. Since the f-phase fraction is not 100%, the P_r normally is much smaller than theoretically predicted. The polarization magnitude of multiphase HfO$_2$ follows the same trend as the f-phase fraction (Supplementary Fig. 6b), consistent with the behavior of P_r in the La-doped HfO$_2$ thin films[23]. Moreover, due to the presence of holes, the P_r of La-doped HZO films is larger than that of HZO films[24].

Origin mechanism of hafnia ferroelectricity

To understand the microscopic mechanism of how carriers stabilize f-phase, we plotted the density of states (DOS) for the c-, f-, and m-phases with $p = 0.2$ h$^+$/f.u. in Fig. 3a–c. In the c-phase, the holes are uniformly distributed in the O^{IV} atom (Fig. 3a), while in the f-phase, the holes preferentially occupy O^{III} atoms, and then are slightly distributed in the O^{IV} atom (Fig. 3b). Similar hole distribution patterns are also reflected in the m-, t-, and o-phase (Fig. 3c and Supplementary Fig. 7). Compared with the DOS
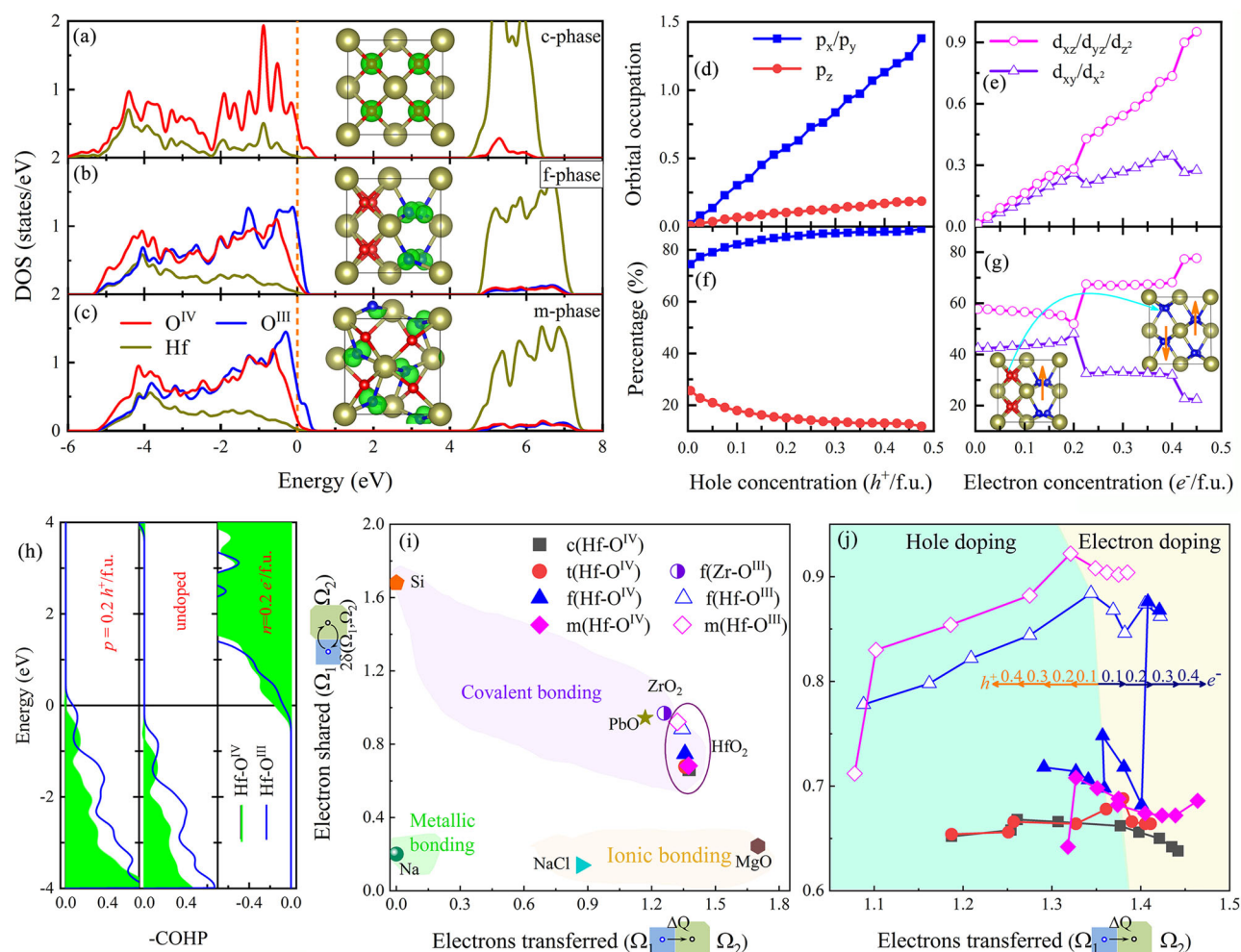
Fig. 3 | Electronic structure and bonding analysis. The atomic density of states (DOS) and 3D charge density distribution of the bulk HfO_2 with hole concentration of 0.2 h^+/f.u., (**a**) c-phase, (**b**) f-phase, (**c**) m-phase, the orange-yellow vertical dashed line represents the Fermi level (E_F). The green isosurface demonstration of charge density distributions of the doping holes is drawn with the same scale in the inserted pictures. In-plane and out-of-plane orbital occupation number and proportion of f-phase HfO_2 as a function of carrier concentration, (**d**), (**f**) hole doping, (**e**), (**g**) electron doping, the structural snapshots in the inset (**g**) show that the transformation of O^{IV} to O^{III} at high electron concentrations with the exact opposite polar to neighboring O^{III}. (**h**) Negative crystal orbital Hamiltonian population (COHP) for

Hf-O bond of f-phase HfO_2 with different carrier concentrations. The COHP is determined by weighting the electronic DOS with the Hamiltonian elements corresponding to orbital overlaps, which divides DOS by energy into bonding, anti-bonding, and non-bonding regions. The convention is to plot negative COHP (-COHP, which is dimensionless). Hence bonding interactions and anti-bonding interactions are positive and negative, respectively. The number of electrons transferred (x-axis) and shared (y-axis) between adjacent basins intuitively illustrates electronic interactions of bonds in materials; they serve as quantitative measures of ionic and covalent properties, respectively. **i** A 2D map of different bonds in different materials and (**j**) Hf-O bonds with different carrier concentrations.

of the m-phase and f (o) phase, the holes of the m-phase are more concentrated in the O^{III} atom. Such a hole distribution pattern does not change unless a phase structure transition occurs (Supplementary Fig. 8).

We mentioned earlier that symmetry is not the main factor that determines the total energy decrease slope. Judging from the perspective of the hole distribution pattern, it seems to indicate that the holes on the O^{IV} atoms are the main factor for determining the total energy decrease slope in each phase. The total energy of the c-phase with more holes distributed on the O^{IV} atoms declines rapidly, while few holes occupied the O^{IV} atoms in the m-phase, making its slope the slowest (Supplementary Tab. 2). The most direct evidence comes from the m′-phase, which has lower symmetry than the c-phase, but its hole concentration on the O^{IV} atoms is twice as high as that of the c-phase (Supplementary Tab. 2), so m′-phase has the steepest slope in Supplementary Fig. 1. Therefore, a ground-state phase transition from m → f (o)→ c (t)→ m′ was observed. For n-type doping, since electrons occupy all the Hf atoms in each phase (Supplementary Fig. 9), and increasing electron doping only increases the number of electrons on the Hf atoms without changing the electron distribution pattern (Supplementary Fig. 10), even if the f-phase undergoes a phase transition.

Gauss' law stipulates that, in electrostatic equilibrium with effective charge screening, the net electric field within a conductor is zero[30]. Puggioni et al.[57] attributed the coexistence of polarity and metallicity to the weak coupling between carriers near the Fermi level and the (soft) phonon(s) responsible for removing inversion symmetry. The number of holes (electrons) occupying the O 2p (Hf 5 d) orbitals is calculated by integrating the DOS near the Fermi level[58]. In Fig. 3d, it is evident that the holes predominantly occupy the in-plane p_x/p_y orbitals. Although the number of holes occupying the p_z orbitals increases slowly, the proportion decreases all the time (Fig. 3f). The difficulty of in-plane holes to eliminate the out-of-plane dipoles generated by the non-centrosymmetric structure results in a weak coupling between the holes and the polarization distortion, thereby exhibiting strong ferroelectricity. However, it is important to acknowledge that, at excess concentrations, a considerable number of holes still occupy the p_z orbital. This phenomenon explains why the P_s has to decrease after a slow increase, reaching its maximum until it eventually drops to zero at a critical concentration (Fig. 2e).

In Fig. 3e, the number of electrons occupied by the out-of-plane d_{xz}/d_{yz}/d_{z^2} orbitals steadily rises with increasing electron concentration,

the heightened electron screening effect propels the metastable f-phase to transform into the antipolar f''-phase at a critical concentration. Due to the inversion symmetry, the proportion of in-plane and out-of-plane orbital electrons remains unchanged after the phase transition (Fig. 3g). Excessive out-of-plane electrons intensify the electron screening effect, making it increasingly difficult to reverse f''-phase.

Alongside electrostatic screening of carriers, chemical bonding arguments can also serve as a framework for understanding the intricate interplay between polar distortion and free carriers[34]. Notably, strong Ti-O covalent bonding[59] has been identified as a significant factor in the lattice instability of $ATiO_3$ (A = Ba, Pb). Moreover, robust Pb-O covalent bonding[60] is considered to be the key factor that leads to the stronger ferroelectricity of $PbTiO_3$ compared to $BaTiO_3$. In Fig. 3h, undoped HfO_2 being an insulator, positions the Fermi level in the Hf-O non-bonding region. Hole doping shifts the Fermi level into the Hf-O^{III} bonding region, fostering stronger Hf-O^{III} covalent bonding. However, concerning the Hf-O^{IV} bond, the Fermi level occupies a lower position on the -COHP curve, residing in the very weak Hf-O^{IV} anti-bonding region. This indicates that hole doping has minimal impact on the properties of the Hf-O^{IV} bond, even when holes predominantly distributed on the O^{IV} atom of t-phase (Supplementary Fig. 11). With electron doping, the Fermi level falls within both the Hf-O^{III} and Hf-O^{IV} anti-bonding regions, but the Hf-O^{IV} anti-bonding region is more extensive. This renders the Hf-O^{IV} bond more unstable compared to the Hf-O^{III} bond. Consequently, during the f-phase transition, it is O^{IV} that moves rather than O^{III} (Fig. 3g), resulting in the formation of the f''-phase instead of the t-phase.

The transition between covalent and ionic bonds is gradual and lacks clear delineated. Recently developed quantum mechanical descriptions of shared electrons and transferred electrons have effectively addressed this issue, culminating in a 2D diagram for analyzing chemical bonds in solid materials[61,62]. Figure 3i offers an intuitive depiction, identifying the fundamental properties of ionic, metallic, and covalent bonds in a compound. Taking the example of binary oxides MgO, the relatively higher electrons transferred (ET) and few electrons shared (ES) in Mg-O bonds, underscore strong ionic bond properties. Whereas for Si, the ES in Si-Si bonds are overwhelmingly dominant, with virtually no ET, which signifies very strong covalent bond properties.

In Fig. 3i, the presence of more ES in the Hf-O^{III} bond in undoped HfO_2, suggests that Hf-O^{III} covalent bonds are considerably stronger than Hf-O^{IV} covalent bonds, a characteristic that favors hafnia ferroelectricity. Furthermore, Zr-O^{III} covalent bonds are stronger than Hf-O^{III} covalent bonds, potentially contributing to the enhancement of ferroelectricity with Zr doping. In Fig. 3j, under p-type doping, there is minimal change in ET and ES of Hf-O^{IV} bonds. While the ES of Hf-O^{III} bonds in the f-phase experiences a slight decrease, the ET undergoes a significant reduction, resulting in an increased ES/ET ratio (Supplementary Fig. 12). Thus, the f-phase can still maintain strong Hf-O^{III} covalent bonds, a favorable condition for ferroelectricity. At low electron concentrations, the ES of Hf-O^{IV} bond decreases not only faster than that of Hf-O^{III} bond in the f-phase but also faster than that of Hf-O^{IV} bond of other phases, which is consistent with the anti-bonding states in Fig. 3h.

For real element doping, our previous studies have shown that II- and III-valent elements, which introduce holes, can stabilize the ferroelectric f-phase of hafnia, while V-valent elements that introduce electrons have the opposite effect[63]. IV-valent dopants, which do not introduce carriers, generally have minimal impact on f-phase stability, in line with findings by Künneth et al.[64] Zr is the most widely studied dopant because Zr is structurally similar to Hf, allowing the formation of solid solutions with a wide range of Hf:Zr atomic ratios. However, from the perspective of phase energy, numerous theoretical studies[21,63–65] of bulk HfO_2 consistently shown that Zr doping has little effect on the phase energy difference ($\Delta E^{f\text{-}m}/\Delta E^{t\text{-}m}$) between the f-phase/t-phase and the m-phase, regardless of the Zr doping position or concentration. The origin of ferroelectricity in Zr-doped HfO_2 films is complex, involving various factors, including oxygen vacancies[15], surface energy[16], annealing temperature, and grain size[65], etc. Another commonly

used IV-valence dopant, Si, induces ferroelectricity in HfO_2 due to its small ionic radius that favors the t-phase[42]. As the Si doping concentration increases, the $\Delta E^{t\text{-}m}$ decreases significantly, stabilizing the t-phase. As mentioned earlier, the t-phase at the crystallization temperature, allowing a phase transition to the f-phase during the cooling process by kinetic effects within the appropriate doping concentration range[25].

To determine the key characteristic parameters that affect the stability of the doped HfO_2 ferroelectric f-phase, we investigated 21 dopants spanning II, III, IV, and V-valent elements across the periodic table, as shown in Supplementary Fig. 13a. Six properties (Supplementary Tab. 3)—carrier concentration, ionic radius, atomic radius, electronegativity, ionization energy, and electron affinity as input variable sets (descriptors), while the energy difference $\Delta E^{f\text{-}m}$ as the observed value, grouped by valence state, and principal component analysis (PCA) was performed[66]. The scree plot (Supplementary Fig. 13b) shows that the first principal component (PC1) can explain 70.8% of the variance in the original descriptor, which means that PC1 can capture most of the changes in the data. The inclusion of the second principal component (PC2) can explain 87.5% of the variance in the descriptor data, indicating that they have captured the main trend of most variables.

In the loading plot (Supplementary Fig. 13c), PC1 and PC2 are primarily influenced by carrier concentration and ionization energy. In PC1, the most significant component, carrier concentration, is positively correlated, while ionization energy is negatively correlated. Since hole concentration is designated as positive in our carrier data, a higher hole concentration correlates with enhanced stability of the ferroelectric phase, while lower ionization energy also promotes this stability. The other four variables contribute less, with atomic and ionic radii positively correlated and electronegativity and electron affinity also showing a positive correlation with ionization energy.

Combining the load plot (Supplementary Fig. 13c) and the score plot (Supplementary Fig. 13d), we observe that the major axis of the IV-valent element ellipse aligns with the direction of ionization energy, indicating that IV-valent elements are strongly influenced by ionization energy. Dopants with lower ionization energy tend to stabilize the ferroelectric phase. For II and III-valent elements, their sample points cluster along the positive PC1 axis with some overlap, reflecting their similar behavior. The carrier load value in the positive PC1 axis is the highest, showing that the phase energy difference under II- and III-valent doping is primarily influenced by carriers. Moreover, the relatively scattered distribution of these scores suggests that ionic radius also contributes to the phase energy difference. Furthermore, because II-valent elements introduce more holes than III-valent elements, II-valent elements score higher than III-valent elements. Since electron concentration is marked as negative, V-valent element samples are mostly located in the third quadrant, with their ellipse's major axis opposite to the carrier direction in the load plot, suggesting that V-valent elements are more sensitive to carrier concentration.

## Interface carrier effect in hafnia-based films

Epitaxial atomic-scale interface with polar catastrophes creates unique phenomena, such as the formation of two-dimensional electron/hole gas (2DEG/2DHG)[67–69]. Shi et al.[37] recently unveiled that hole doping in the HZO layer, resulting from the MnO_2 interface termination in HZO/$La_{0.67}Sr_{0.33}MnO_3$ thin film, stably reduces the clear ferroelectric features to a 1.5 nm thick HZO. Additionally, Cheema et al.[39] demonstrate ferroelectricity in a 1 nm HZO ultrathin film grown by low-temperature atomic layer deposition (ALD) on Si/SiO_2. Subsequently, Cheema et al.[70,71] also found that the thickness of ferroelectric ZrO_2 films and HfO_2-ZrO_2 multilayer could be maintained at 0.5 nm and 2 nm, indicating an inverse size effect for hafnia-based films. Its structural characterization shows that only metal-oxygen dangling bonds are present out-of-plane. But as we know, these metal-oxygen dangling bonds inevitably bring surface or interfacial holes. As we mentioned earlier, holes can enhance the ferroelectricity of bulk hafnia, so here we further explore the effect of holes on the ferroelectric properties of f-phase HfO_2 thin films. In Supplementary Fig. 14,
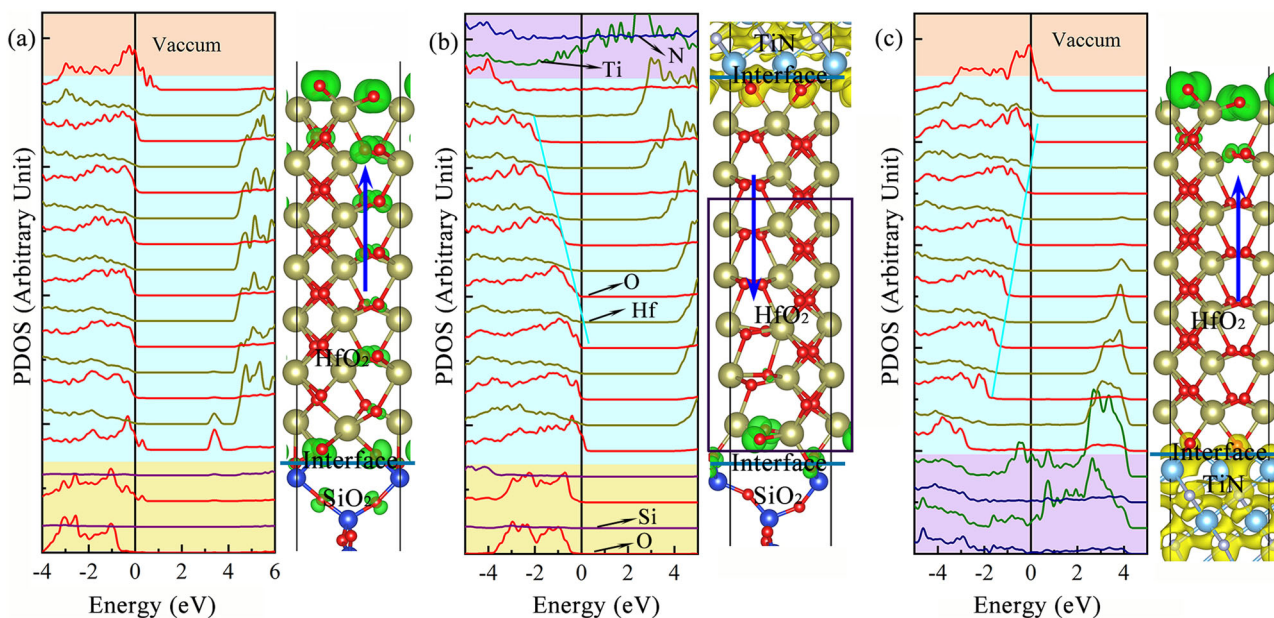
Fig. 4 | The layer-resolved DOS of HfO₂-based HS. Calculated layer-resolved DOS along with its 3D charge density projected on the bands forming the metallic states near the Fermi level for (**a**) SiO$_2$/f-HfO$_2$, (**b**) SiO$_2$/f-HfO$_2$/TiN, (**c**) TiN/f-HfO$_2$ HS models. Since the coordination number of some O atoms cannot be determined after relaxation, the different types of O atoms are no longer distinguished by color in the HfO$_2$-based HS. The holes and electrons are depicted by green and yellow iso-surfaces, respectively. The blue arrows indicate the direction of polarization, which is directed along the line from the negative charge toward the positive charge. The cyan line represents the electrostatic potential. The purple box in (**b**) shows a thickness of 1 nm.
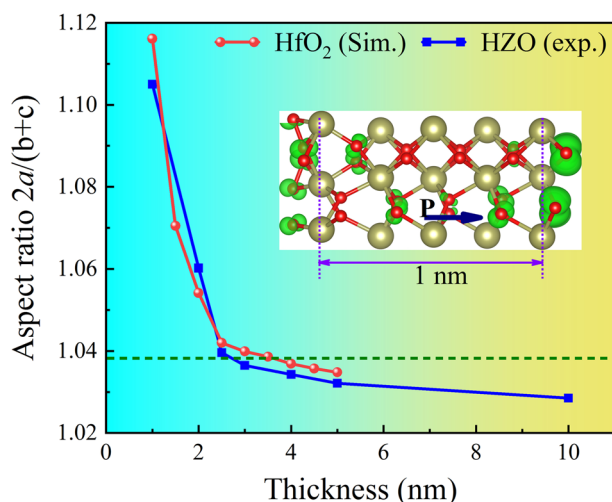
Fig. 5 | Aspect ratio of different thicknesses. Aspect ratio $2a/(b + c)$ as a function of HfO$_2$ film thickness, with experimental HZO film as comparison[39]. Dashed line represents the aspect ratio of bulk f-phase HfO$_2$. The inset shows the 3D hole distribution in the 1 nm HfO$_2$ ultra-film.

constructing several models of SiO$_2$/f-HfO$_2$ and TiN/f-HfO$_2$ hetero-structure (HS) with oxygen terminations, capping with or without TiN electrode.

In Supplementary Fig. 14, it is evident that only two O atoms are paired with Si at the SiO$_2$/f-HfO$_2$ interface, while the remaining two dangling O atoms will form a metallic state at the SiO$_2$/f-HfO$_2$ interface, as shown in Fig. 4. Undoubtedly, the most dominant holes in the heterostructures come from the dangling O atoms on the surface. Figure 4a clearly demonstrates that the SiO$_2$/f-HfO$_2$ HS, without being capped with TiN, can still maintain the polar structure at a thickness of 1.5 nm. Essentially, every O layer in f-HfO$_2$ exhibits hole distribution, with a higher concentration on the polar O^{III} atoms, promoting the formation of the f-phase in the HfO$_2$ thin film.

Since the number of holes generated at the interface and the surface remains constant, thinner films have a higher hole concentration and greater polar distortion (Supplementary Fig. 15). In Fig. 5, we observe that the aspect ratio of HfO$_2$ thin films shows nearly exponential growth with decreasing thickness, similar to the trend observed in HZO ultrathin films[39]. Additionally, with the same hole doping, a 3 nm BaTiO$_3$ film exhibits antipolar structure, while a 3 nm HfO$_2$ film maintains a strong polar structure (Supplementary Fig. 16). Shi et al. introduced holes into HfO$_2$-based films through the work function difference at the metal/dielectric layer interface, whereas we utilized dangling oxygen at the interface, indicating that the existence of holes may be one of the reasons for the lack of critical thickness of HfO$_2$-based films. Other methods of introducing holes at an interface also include using the mismatch of interface chemical valence to affect the electrostatic potential at the interface[68].

Because it is not feasible to measure ferroelectricity in metals, the annealed HZO region without metal capping does not exhibit ferro-electric signatures. However, clear PFM phase contrast images emerge on the HZO region with capped metal during phase annealing, and 180° phase contrast and butterfly-shaped amplitude are observed only for metal-capped HZO[39]. This phenomenon is elucidated by the layer-resolved partial DOS in SiO$_2$/f-HfO$_2$/TiN HS (Fig. 4b). Besides forming a metallic state on SiO$_2$/f-HfO$_2$ (p-type) and f-HfO$_2$/TiN (n-type) inter-face layer, the interior of the HfO$_2$ thin film remains insulating. Due to the asymmetry interface, the robust electrostatic potential (cyan line in Fig. 4b) propels the polarization direction switching of the initially constructed structure. Moreover, Cheema et al.[39] showed PFM phase contrast and topographical imaging for 1 nm HZO on TiN-buffered Si without metal capping. Figure 4c illustrates a small number of holes on the surface of the HfO$_2$ film in the TiN/f-HfO$_2$ HS, while the film's interior retains insulation, affirming that the 1 nm HZO on TiN exhibits ferroelectric signatures. Capping with a TiN electrode also leads to n-type conductivity at the top interface, with minimal alterations in the f-phase structure morphology (Supplementary Fig. 17). Moreover, La doping introduces more holes into SiO$_2$/f-HfO$_2$@La HS (Supplementary Fig. 18a), the high hole concentration resulting from the superposition of doped holes and interface holes, may explain the formation of a very thin

interfacial c/t-phase layer in the La-doped[23] and Gd-doped[72] thin films. Once capped with TiN, almost all holes are absorbed (Supplementary Fig. 18b), and even electrons brought by Ta doping are absorbed (Supplementary Fig. 18c), ensuring insulation.

In general, as the TiN top electrode is typically sputter-deposited on already-existing HfO_2-based thin films, the top electrode cannot affect the growth behavior of dielectric layers. We speculate that these carriers play a pivotal role in initiating the formation of the f-phase in the uncapped HfO_2-based films. Once this task is accomplished, in the presence of capped electrodes, these carriers are assimilated by the capping electrodes to maintain charge neutrality within the films. This could explain why, in most instances, capped HfO_2 layers possess better ferroelectricity than those without capping[5]. In addition, this phenomenon is supported by Pt/Ta-doped HfO_2/Pt capacitors[27]. Even with significant Ta doping concentrations (Ta atomic ratio of 11%–21%), strong ferroelectricity can still be measured. Finally and most importantly, due to the limited screening length of the electrodes on charge carriers, hafnia films with strong ferroelectricity can be found to have thicknesses of essentially ~10 nm or less, much smaller than that of perovskite ferroelectric materials. Of course, apart from the compensation with surface charges, the more or less existing oxygen vacancies in the doped HfO_2-based thin film play this role because they can locally neutralize excess charges by generating oxygen vacancy-dopant pairs[8]. In addition, co-doping of n-p type elements can not only achieve charge neutrality but also enhance the ferroelectric properties of hafnia-based films[57,73].

In summary, our first-principles calculations unveil distinct mechanisms underlying the induction of ferroelectricity in hafnia when doped with p-type and n-type dopants. For p-type doping, the holes concentrated on the polar O^{III} atoms in the f-phase significantly enhance robust ferroelectricity, driven by a weak hole screening effect and augmented polar Hf-O^{III} covalent bonds. However, the presence of holes on nonpolar O^{IV} atoms crucially influences the phase total energy change, leading to a ground state m → f → c phase transition as hole concentration increases. As a result, the f-phase fraction and polarization magnitude exhibit an initial increase followed by a decrease. In contrast, n-type doping involves strong electron screening and a weaker Hf-O^{IV} covalent bond, inducing a transition from the polar metastable f-phase to the antipolar stable f″-phase. This distinction might explain the challenges in identifying ferroelectricity in n-type doped hafnia. Lastly, we emphasize the pivotal role of electrode capping in ensuring the ferroelectric insulation of hafnia-based films.

While the internal energy calculated by the standard density-functional theory (DFT) approach has certain limitations in fully capturing the complexity of ferroelectric f-phase stability in hafnia—particularly under the influence of temperature, grain size, and domain structure—our findings are broadly consistent with experimental measurements of doped hafnia films. This alignment underscores the potential of precisely modulating carrier concentration as a promising strategy to significantly enhance the ferroelectric properties of hafnia-based devices.

To further improve the precision and depth of such studies, overcoming current theoretical and computational limitations will be essential. Free energy differences, being more reliable than internal energies alone in predicting ferroelectric phase stability, highlight the potential of advanced computational approaches—such as ab initio molecular dynamics (MD), stochastic self-consistent harmonic approximations (SSCHA), and temperature-dependent effective potential (TDEP) methods. These methods have shown promise in addressing critical factors such as temperature effects and anharmonicity but remain computationally prohibitive for systematically exploring multiple dopants and phases.

Looking ahead, the development of machine-learning-based force-field models presents a compelling opportunity to overcome these challenges. By integrating machine learning with traditional quantum mechanical frameworks, it may become possible to efficiently explore phase stability in doped systems and uncover the intricate mechanisms by which dopants modulate ferroelectric properties. Such advancements could pave

the way for more precise theoretical insights and optimized designs of ferroelectric materials and devices.

Methods

First-principles calculations of bulk structures

We consider five competing phases, including ground nonpolar monoclinic m-phase, cubic c-phases, tetragonal t-phases, polar orthorhombic f-phase, and antipolar orthorhombic o-phase, in this work. Our work is based on DFT as implemented in the Vienna ab initio simulation package (VASP)[74,75], using a plane-wave basis set with a kinetic energy of 500 eV, employing the standard projector-augmented wave (PAW) methodology and the generalized gradient approximation (GGA)[76] parametrized by the Perdew-Burke-Ernzerhof (PBE) exchange-correlation functional. For structure relaxations of each phase hafnia, a $7 \times 7 \times 7$ Gamma-centered k-point meshes are used, all lattice parameters and atomic positions were allowed to relax until the energy differences were within 10^{-6} eV and the Hellman-Feynman forces were less than 0.01 eV/Å. For the DOS calculations, denser k-point meshes with an $11 \times 11 \times 11$ Gamma-centered grid are used. Supplementary Tab. 1 lists the lattice parameters of the five phases of hafnia we used in this work together with previously reported theoretical and experimental results, as predicted by our DFT calculations, which are in good agreement with the experimental data.

We use the smallest cells describing the equilibrium structures of the five phases of hafnia, simulate the effect of doping by varying the number of electrons in the cell, and add a neutralizing homogeneous charge background. Therefore, the doping holes were introduced to the system with a negative background to achieve charge neutrality, while doping electrons did the opposite. This approach does not take into account the fundamental properties of dopant atoms, such as ionic radius, electronegativity, etc., which greatly simplifies calculations and provides insight into the origin of ferroelectricity in p-type and n-type doped hafnia. In addition, crystal orbital Hamilton population (COHP) analyses are carried out with the LOBSTER code[77]. Moreover, the energy barriers for polarization switching are obtained with the aid of the climbing image nudged elastic band (NEB) method. Crystal structures and the isosurfaces of the three-dimensional (3D) charge density are visualized using the VESTA package[78].

The polarization magnitude of f-phase hafnia was calculated by Born effective charges (BEC, Z^*)[79] multiplied by atomic displacements (δd) with respect to the referenced centrosymmetric t-phase. Formally, P_s simply took the form of:

$$P_s = \frac{e}{\Omega} \sum_i Z_i^* \delta d_i \qquad (1)$$

Where i represents the ith atom, e and Ω are the charge of the electron and the cell volume considered, respectively. The BEC along the c-axis derived from density-functional perturbation theory calculations[80]. Our spontaneous polarization $P_s = 58.41$ μC/cm² of undoped f-phase is close to the $P_s = 53.31$ μC/cm² predicted by Zhou et al.[47]

Chemical bond calculations

For analyzing electronic interactions and bonding in materials, the initial DFT wavefunctions were post-processed in Quantum Espresso[81], then followed by a transformation into maximally localized Wannier functions (MLWFs)[82] and integration within the Critic2 code[83].

The integral of the nonclassical exchange-(correlation) part of the electron-pair density function satisfies the summation rule[84]:

$$N(\Omega) = LI(\Omega) + \frac{1}{2} \sum_{\Omega' \neq \Omega} \delta(\Omega', \Omega) \qquad (2)$$

Where the localization index $LI(\Omega)$, measuring the number of electrons that are fully localized in the Bader's basin, depending on the atom type and its specific chemical environment. while the delocalization index $\delta(\Omega', \Omega)$,

measures the number of electron pairs being shared between the two basins, therefore, their double corresponds to the amount of shared electrons (ES). $N(\Omega)$ is the electron population of the Ω atom, and the difference between it and the total number of electrons of Ω atom is expressed as the transferred electron (ET) between two atomic basins.

Heterostructure modeling and calculation

In addition, we constructed SiO_2/HfO_2 HS and $SiO_2/HfO_2/TiN$ HS to explore the influence of interface carriers on the f-phase structure and ferroelectricity. Among them, SiO_2 adopts the most stable crystal structure with space group $I\bar{4}2d$ ($a = b = 4.95$ Å, $c = 7.31$ Å, $\alpha = \beta = \gamma = 90°$) found in the Materials Project web[85], which has a relatively small in-plane lattice mismatch with the f-phase structure. In 2020, Cheema et al.[39] prepared ferroelectric $Si/SiO_2/HZO/TiN$ thin films and used out-of-plane one-dimensional GI-XRD patterns and two-dimensional pole figure patterns to reflect the stacking of the (311) and (111) densely packed planes in the fluorite structure. The results confirmed that all the cation sites lie in-planes, which minimizes surface energy effects because only metal-oxygen dangling bonds are present out-of-plane. So here, both the surface and the interface of the f-phase film in our heterojunction are O-terminated. The TiN adopts the crystal structure of space group $Fm\bar{3}m$ ($a = b = c = 4.22$ Å), to reduce the in-plane lattice mismatch between the TiN electrode and the f-phase hafnia ($a = 5.27$ Å, $b = 5.05$ Å) film, we constructed the TiN electrode along the (111) direction ($a = 5.97$ Å, $b = 5.17$ Å) compared to the (001) direction ($a = b = 4.22$ Å). In addition, TiN in the (111) direction is alternately stacked with Ti terminals and N terminals, which makes it easier to adapt to the O terminals of the f-phase at the interface. We construct SiO_2/f-HfO_2, SiO_2/f-$HfO_2/TiN(111)$, and $TiN(111)/f$-phase HfO_2 HS along the (001) direction with a 20 Å vacuum layer, and fix the in-plane lattice constants of all constructed HS to those of the f-phase. The 6×6×1 k-mesh and Hellman-Feynman forces were less than 0.05 eV/Å are used in VASP calculation.

Data availability

The authors declare that the data supporting the findings of this study are available within the article and its supplementary information files or from the corresponding authors on reasonable request.

Code availability

The central codes used in this paper are VASP and Quantum ESPRESSO.

References

1. Böscke, T. S., Müller, J., Bräuhaus, D., Schröder, U. & Böttger, U. Ferroelectricity in hafnium oxide thin films. *Appl. Phys. Lett* **99**, 102903 (2011).
2. Wu, Y. et al. Unconventional polarization-switching mechanism in (Hf, Zr)O₂ ferroelectrics and its implications. *Phys. Rev. Lett.* **131**, 226802 (2023).
3. Yan, S. et al. Recent progress in ferroelectric synapses and their applications. *Sci. China Mater.* **66**, 877–894 (2023).
4. Li, Z. et al. Ferroelectric hafnium oxide films for in-memory computing applications. *Adv. Electron. Mater.* **8**, 2200951 (2022).
5. Yang, W. et al. Ferroelectricity of hafnium oxide-based materials: current status and future prospects from physical mechanisms to device applications. *J. Semicond.* **44**, 053101 (2023).
6. Ohtaka, O. et al. Phase relations and volume changes of hafnia under high pressure and high temperature. *J. Am. Cer. Am. Soc.* **84**, 1369–1373 (2001).
7. Ohtaka, O. et al. Phase relations and equations of state of ZrO₂ under high temperature and high pressure. *Phys. Rev. B* **63**, 174108 (2001).
8. Schroeder, U., Hwang, C. S., Funakubo, H. (eds). Ferroelectricity in doped hafnium oxide: Materials, properties and devices (Woodhead Publishing, 2019).
9. Hoffmann, M. et al. Stabilizing the ferroelectric phase in doped hafnium oxide. *J. Appl. Phys.* **118**, 072006 (2015).
10. Starschich, S. & Boettger, U. An extensive study of the influence of dopants on the ferroelectric properties of HfO₂. *J. Mater. Chem. C* **5**, 333–338 (2017).
11. Park, M. H. et al. A comprehensive study on the structural evolution of HfO₂ thin films doped with various dopants. *J. Mater. Chem. C* **5**, 4677–4690 (2017).
12. Xu, X. et al. Kinetically stabilized ferroelectricity in bulk single-crystalline HfO₂:Y. *Nat. Mater.* **20**, 826–832 (2021).
13. Pal, A. et al. Enhancing ferroelectricity in dopant-free hafnium oxide. *Appl. Phys. Lett.* **110**, 022903 (2017).
14. Zhou, Y. et al. The effects of oxygen vacancies on ferroelectric phase transition of HfO₂-based thin film from first-principle. *Comp. Mater. Sci.* **167**, 143–150 (2019).
15. Wei, J., Jiang, L., Huang, M., Wu, Y. & Chen, S. Intrinsic defect limit to the growth of orthorhombic HfO₂ and (Hf,Zr)O₂ with strong ferroelectricity: first-principles insights. *Adv. Funct. Mater.* **31**, 2104913 (2021).
16. Materlik, R., Künneth, C. & Kersch, A. The origin of ferroelectricity in Hf₁₋ₓZrₓO₂: a computational investigation and a surface energy model. *J. Appl. Phys.* **117**, 134109 (2015).
17. Batra, R., Tran, H. D. & Ramprasad, R. Stabilization of metastable phases in hafnia owing to surface energy effects. *Appl. Phys. Lett.* **108**, 172902 (2016).
18. Kim, S. J. et al. Large ferroelectric polarization of TiN/Hf₀.₅Zr₀.₅O₂/TiN capacitors due to stress-induced crystallization at low thermal budget. *Appl. Phys. Lett.* **111**, 242901 (2017).
19. Zhang, Y., Yang, Q., Tao, L., Tsymbal, E. Y. & Alexandrov, V. Effects of strain and film thickness on the stability of the rhombohedral phase of HfO₂. *Phys. Rev. Appl.* **14**, 014068 (2020).
20. Schroeder, U., Park, M. H., Mikolajick, T. & Hwang, C. S. The fundamentals and applications of ferroelectric HfO₂. *Nat. Rev. Mater.* **7**, 653–669 (2022).
21. Batra, R., Huan, T. D., Rossetti, G. A. Jr & Ramprasad, R. Dopants promoting ferroelectricity in hafnia: insights from a comprehensive chemical space exploration. *Chem. Mater.* **29**, 9102–9109 (2017).
22. Materlik, R., Künneth, C., Falkowski, M., Mikolajick, T. & Kersch, A. Al-, Y-, and La-doping effects favoring intrinsic and field induced ferroelectricity in HfO₂: a first principles study. *J. Appl. Phys.* **123**, 164101 (2018).
23. Schroeder, U. et al. Lanthanum-doped hafnium oxide: a robust ferroelectric material. *Inorg. Chem.* **57**, 2752–2765 (2018).
24. Chernikova, A. G. et al. Improved ferroelectric switching endurance of La-doped Hf₀.₅Zr₀.₅O₂ thin films. *ACS Appl. Mater. Interfaces* **10**, 2701–2708 (2018).
25. Mimura, T., Shimizu, T., Sakata, O. & Funakubo, H. Large thermal hysteresis of ferroelectric transition in HfO₂-based ferroelectric films. *Appl. Phys. Lett.* **118**, 112903 (2021).
26. Park, M. H., Lee, Y. H. & Hwang, C. S. Understanding ferroelectric phase formation in doped HfO₂ thin films based on classical nucleation theory. *Nanoscale* **11**, 19477–19487 (2019).
27. Luo, C. Q., Kang, C. Y., Song, Y. L., Wang, W. P. & Zhang, W. F. Large remanent polarization in Ta-doped HfO₂ thin films by reactive sputtering. *Appl. Phys. Lett.* **119**, 042902 (2021).
28. Fang, Y. W. & Chen, H. Design of a multifunctional polar metal via first-principles high-throughput structure screening. *Commun. Mater.* **1**, 1024 (2020).
29. Paredes Aulestia, E. I. et al. Pressure-induced enhancement of non-polar to polar transition temperature in metallic LiOsO₃. *Appl. Phys. Lett.* **113**, 012902 (2018).
30. Fei, Z. et al. Ferroelectric switching of a two-dimensional metal. *Nature* **560**, 336–339 (2018).
31. Jiao, Y. et al. Coupled magnetic and structural phase transitions in the antiferromagnetic polar metal Pb₂CoOsO₆ under pressure. *Phys. Rev. B* **102**, 144418 (2020).

32. Kolodiazhnyi, T., Tachibana, M., Kawaji, H., Hwang, J. & Muromachi, E. T. Persistence of ferroelectricity in BaTiO$_3$ through the insulator-metal transition. *Phys. Rev. Lett.* **104**, 147602 (2010).

33. Wang, Y., Liu, X., Burton, J. D., Jaswal, S. S. & Tsymbal, E. Y. Ferroelectric instability under screened Coulomb interactions. *Phys. Rev. Lett.* **109**, 247601 (2012).

34. Zhao, H. J. et al. Meta-screening and permanence of polar distortion in metallized ferroelectrics. *Phys. Rev. B.* **97**, 054107 (2018).

35. Young, D. H., Puggioni, D. & Rondinelli, J. M. Persistent polar distortions from covalent interactions in doped BaTiO$_3$. *Phys. Rev. B* **102**, 014108 (2020).

36. Li, G. et al. Coexistence of ferroelectricity and metallicity in M-doped BaTiO3 (M = Al, V, Cr, Fe, Ni, and Nb): first-principles study. *Mater. Today Commun.* **27**, 102394 (2021).

37. Cao, T., Ren, G., Shao, D. F., Tsymbal, E. Y. & Mishra, R. Stabilizing polar phases in binary metal oxides by hole doping. *Phys. Rev. Mater.* **7**, 044412 (2023).

38. Shi, S. et al. Interface-engineered ferroelectricity of epitaxial Hf$_{0.5}$Zr$_{0.5}$O$_2$ thin films. *Nat. Commun.* **14**, 1780 (2023).

39. Cheema, S. S. et al. Enhanced ferroelectricity in ultrathin films grown directly on silicon. *Nature* **580**, 478–482 (2020).

40. Clima, S. et al. *IEEE International Electron Devices Meeting (IEDM)* 4.2.1–4.2.4 (IEEE, 2020).

41. Fan, S. T., Chen, Y. W. & Liu, C. W. Strain effect on the stability in ferroelectric HfO$_2$ simulated by first-principles calculations. *J. Phys. D Appl. Phys.* **53**, 23LT01 (2020).

42. Lee, C. K., Cho, E., Lee, H. S., Hwang, C. S. & Han, S. First-principles study on doping and phase stability of HfO$_2$. *Phys. Rev. B* **78**, 012102 (2008).

43. Schlom, D. G. et al. Elastic strain engineering of ferroic oxides. *MRS Bull.* **39**, 118–130 (2014).

44. Shiraishi, T. et al. Impact of mechanical stress on ferroelectricity in (Hf$_{0.5}$Zr$_{0.5}$)O$_2$ thin films. *Appl. Phys. Lett.* **108**, 262904 (2016).

45. Park, M. H., Kim, H. J., Kim, Y. J., Moon, T. & Hwang, C. S. The effects of crystallographic orientation and strain of thin Hf$_{0.5}$Zr$_{0.5}$O$_2$ film on its ferroelectricity. *Appl. Phys. Lett.* **104**, 072901 (2014).

46. Xu, L. et al. Kinetic pathway of the ferroelectric phase formation in doped HfO$_2$ films. *J. Appl. Phys.* **122**, 124104 (2017).

47. Wei, W. et al. Switching pathway-dependent strain-effects on the ferroelectric properties and structural deformations in orthorhombic HfO$_2$. *J. Appl. Phys.* **131**, 154101 (2022).

48. Zhou, S., Zhang, J. & Rappe, A. M. Touch IoT enabled by wireless self-sensing and haptic-reproducing electronic skin. *Sci. Adv.* **8**, eadd5953 (2022).

49. Choe, D. H. et al. Unexpectedly low barrier of ferroelectric switching in HfO$_2$ via topological domain walls. *Mater. Today* **50**, 8–15 (2021).

50. Henkelman, G. & Jónsson, H. A climbing image nudged elastic band method for finding saddle points and minimum energy paths. *J. Chem. Phys.* **113**, 9901–9904 (2000).

51. Henkelman, G. & Jónsson, H. Improved tangent estimate in the nudged elastic band method for finding minimum energy paths and saddle points. *J. Chem. Phys.* **113**, 9978–9985 (2000).

52. Li, S. & Birol, T. Suppressing the ferroelectric switching barrier in hybrid improper ferroelectrics. *npj Comput. Mater.* **6**, 168 (2020).

53. Clima, S. et al. Identification of the ferroelectric switching process and dopant-dependent switching properties in orthorhombic HfO2: a first principles insight. *Appl. Phys. Lett.* **104**, 092906 (2014).

54. Wang, Y. et al. A stable rhombohedral phase in ferroelectric Hf(Zr)$_{1+x}$O$_2$ capacitor with ultralow coercive field. *Science* **381**, 558–563 (2023).

55. Ma, C., Jin, K. J., Ge, C. & Yang, G. Z. Strain-engineering stabilization of BaTiO$_3$ -based polar metals. *Phys. Rev. B.* **97**, 115103 (2018).

56. Lu, J. et al. Ferroelectricity with asymmetric hysteresis in metallic LiOsO$_3$ ultrathin films. *Phys. Rev. Lett.* **122**, 227601 (2019).

57. Puggioni, D. & Rondinelli, J. M. Designing a robustly metallic noncentrosymmetric ruthenate oxide with large thermopower anisotropy. *Nat. Commun.* **5**, 3432 (2014).

58. Nazir, S. & Yang, K. First-principles characterization of the critical thickness for forming metallic states in strained LaAlO$_3$/SrTiO$_3$(001) heterostructure. *ACS Appl. Mater. Interfaces* **6**, 22351–8 (2014).

59. Cohen, R. E. Origin of ferroelectricity in perovskite oxides. *Nature* **358**, 136–138 (1992).

60. Kuroiwa, Y. et al. Evidence for Pb-O covalency in tetragonal PbTiO$_3$. *Phys. Rev. Lett.* **87**, 217601 (2001).

61. Raty, J. Y. et al. A quantum-mechanical map for bonding and properties in solids. *Adv. Mater.* **31**, 1806280 (2019).

62. Ronneberger, I., Zanolli, Z., Wuttig, M. & Mazzarello, R. Changes of structure and bonding with thickness in chalcogenide thin films. *Adv. Mater.* **32**, 2001033 (2020).

63. Li, G. et al. Charge-compensated co-doping stabilizes robust hafnium oxide ferroelectricity. *J. Mater. Chem. C* **12**, 6257–6266 (2024).

64. Künneth, C., Materlik, R., Falkowski, M. & Kersch, A. Impact of four-valent doping on the crystallographic phase formation for ferroelectric HfO$_2$ from first-principles: implications for ferroelectric memory and energy-related applications. *ACS Appl. Nano Mater.* **1**, 254–264 (2017).

65. Ye, K. H. et al. Comprehensive interpretations of thermodynamic and kinetic effects on the phase fractions in Hf$_{1-x}$Zr$_x$O$_2$ by first principle calculations. *Appl. Phys. Rev.* **10**, 031419 (2023).

66. Maćkiewicz, A. & Ratajczak, W. Maćkiewicz, A. & Ratajczak, W. Principal components analysis (PCA). *Comp. Geosci.* **19**, 303–342 (1993).

67. Ohtomo, A. & Hwang, H. Y. A high-mobility electron gas at the LaAlO$_3$/SrTiO$_3$ heterointerface. *Nature* **427**, 423–6 (2004).

68. Lee, H. et al. Direct observation of a two-dimensional hole gas at oxide interfaces. *Nat. Mater.* **17**, 231–236 (2018).

69. Cheng, J. & Yang, K. Design of two-dimensional electron gas systems via polarization discontinuity from large-scale first-principles calculations. *J. Mater. Chem. C* **6**, 6680–6690 (2018).

70. Cheema, S. S. et al. Ultrathin ferroic HfO$_2$–ZrO$_2$ superlattice gate stack for advanced transistors. *Nature* **604**, 65–71 (2022).

71. Cheema, S. S. et al. Emergent ferroelectricity in subnanometer binary oxide films on silicon. *Science* **376**, 648–652 (2022).

72. Neaton, J. B., Ederer, C., Waghmare, U. V., Spaldin, N. A. & Rabe, K. M. Structural changes underlying field-cycling phenomena in ferroelectric HfO$_2$ thin films. *Adv. Electron. Mater.* **2**, 1600173 (2016).

73. Zhou, C. et al. Enhanced polarization switching characteristics of HfO$_2$ ultrathin films via acceptor-donor co-doping. *Nat. Commun.* **15**, 2893 (2024).

74. Kresse, G. & Furthmüller, J. Efficient iterative schemes for ab initio total-energy calculations using a plane-wave basis set. *Phys. Rev. B* **54**, 11169–11186 (1996).

75. Kresse, G. & Joubert, D. From ultrasoft pseudopotentials to the projector augmented-wave method. *Phys. Rev. B* **59**, 1758–1775 (1999).

76. Perdew, J. P., Burke, K. & Ernzerhof, M. Generalized gradient approximation made simple. *Phys. Rev. Lett.* **77**, 3865–3868 (1996).

77. Maintz, S., Deringer, V. L., Tchougréeff, A. L. & Dronskowski, R. LOBSTER: a tool to extract chemical bonding from plane-wave based DFT. *J. Comput. Chem.* **37**, 1030–5 (2016).

78. Momma, K. & Izumi, F. VESTA: a three-dimensional visualization system for electronic and structural analysis. *J. Appl. Crystallogr.* **41**, 653–658 (2008).

79. Neaton, J. B., Ederer, C., Waghmare, U. V., Spaldin, N. A. & Rabe, K. M. First-principles study of spontaneous polarization in multiferroic BiFeO$_3$. *Phys. Rev. B* **71**, 014113 (2005).

80. Baroni, S., Giannozzi, P. & Testa, A. Green's-function approach to linear response in solids. *Phys. Rev. Lett.* **58**, 1861–1864 (1987).

81. Giannozzi, P. et al. QUANTUM ESPRESSO: a modular and open-source software project for quantum simulations of materials. *J. Phys. Condens. Mat.* **21**, 395502 (2009).
82. Mostofi, A. A. et al. wannier90: a tool for obtaining maximally-localised Wannier functions. *Comput. Phys. Commun.* **178**, 685–699 (2008).
83. Otero-de-la-Roza, A., Blanco, M. A., Pendás, A. M. & Luaña, V. Critic: a new program for the topological analysis of solid-state electron densities. *Comput. Phys. Commun.* **180**, 157–166 (2009).
84. Golub, P. & Baranov, A. I. Domain overlap matrices from plane-wave-based methods of electronic structure calculation. *J. Chem. Phys.* **145**, 154107 (2016).
85. Jain, A. et al. Commentary: The Materials Project: A materials genome approach to accelerating materials innovation. *APL Mater* **1**, 011002 (2013).

Author contributions
M.T. and Z.L. proposed and supervised the project. G.L. and S.Y. designed the method to investigate the carrier doping effect in hafnia based on extensive experimental results. G.L. implemented the computational scheme, analyzed and processed the data, and wrote the manuscript. J.L. contributed to the design and improvement of the calculation scheme, and the revision of the manuscript. Y.L. and W.Z. contributed to the design of the modeling of the hafnia-based heterostructures in the calculations and provided reasonable suggestions for the calculations. Y.X. and Q.Y. contributed to the data analysis and the revision of the manuscript. All authors have approved the final version of the manuscript.

Competing interests
The authors declare no competing interests.

Additional information
Supplementary information The online version contains supplementary material available at https://doi.org/10.1038/s41524-025-01515-7.

Correspondence and requests for materials should be addressed to Minghua Tang, Jiangyu Li or Zhilin Long.

Reprints and permissions information is available at http://www.nature.com/reprints

Publisher's note Springer Nature remains neutral with regard to jurisdictional claims in published maps and institutional affiliations.